Materials Today 99 (2026) 103450

Contents lists available at ScienceDirect

Materials Today

journal homepage: www.elsevier.com/locate/mattod

Designing chemically adaptive nanolaminates via oxygen dynamic partitioning

Xiaolong Yu [a,b,1], Guodong Sun [a,b,1], Daniel Şopu [c,d], Lukas Schretter [c,e], Christoph Gammer [c], Yifeng Li [f], Ge Wu [g,**], Chang Liu [g], Yandong Jia [a,b,*], Jürgen Eckert [c,e], Yong Yang [h], Yang Lu [i,***], Gang Wang [a,b], Xilei Bian [a,b,*]

[a] State Key Laboratory of Materials for Advanced Nuclear Energy, Shanghai University, Shanghai 200444, China
[b] Zhejiang Institute of Advanced Materials, Shanghai University, Jiashan 314100, China
[c] Erich Schmid Institute of Materials Science, Austrian Academy of Sciences, Jahnstraße 12, 8700 Leoben, Austria
[d] Materials Modelling, Institute of Materials Science, Darmstadt University of Technology, Otto-Berndt-Straße 3, 64287 Darmstadt, Germany
[e] Department of Materials Science, Chair of Materials Physics, Technical University of Leoben, Jahnstraße 12, 8700 Leoben, Austria
[f] Laboratory for Microstructures, Shanghai University, Shanghai 200444, China
[g] State Key Laboratory for Mechanical Behavior of Materials, Xi'an Jiaotong University, Xi'an 710049, China
[h] Department of Mechanical Engineering, College of Engineering, City University of Hong Kong, Hong Kong 999077, China
[i] Department of Mechanical Engineering, The University of Hong Kong, Hong Kong 999077, China

A B S T R A C T

Crystalline-amorphous nanolaminates (C/A NLs) have long been conceived as static composites, with their performance predetermined by layer thickness and phase fractions. Here, we introduce a paradigm shift that transforms these materials into chemically adaptive systems through oxygen dynamic partitioning. By harnessing interstitial oxygen as an in-situ chemical modulator, we show that NLs can reconfigure their local chemistry during deformation, evolving from a preset structure into a self-optimizing system. We realize this concept in FeCrNi-O/TiVNbHf-O NLs, where deformation drives oxygen redistribution from the amorphous layers and interfaces to the crystalline layers, increasing oxygen content by 1.55 at.% and amplifying intralayer chemical inhomogeneity without forming oxides. This dynamic chemical evolution progressively strengthens the crystalline phase, reduces the mechanical mismatch between the two layers, and facilitates coordinated deformation throughout the entire architecture. As a result, the two phases achieve a dynamic convergence in mechanical behavior, not by design but by evolution. This chemo-mechanical coupling yields exceptional performance, delivering an ultrahigh yield strength ($\sim E/30$, approaching the theoretical limit $\sim E/10$) alongside a homogeneous compressive strain exceeding 50%, with no shear band formation. The approach is broadly applicable across alloy systems and establishes chemical reconfiguration as a new design paradigm for materials that adapt rather than merely serve as passive constituents.

Introduction

Nanocrystalline metals and metallic glasses (MGs) typically exhibit high strength but limited homogeneous deformation [1,2]. Their crystalline–amorphous nanolaminates (C/A NLs), by contrast, combine high strength with considerable plasticity [3–5]. In these layered architectures, the crystalline–amorphous interfaces (CAIs) function as both efficient dislocation sources and high-capacity sinks, suppressing strain localization in the crystalline phase while activating distributed shear transformation zones (STZs) in the amorphous layers through dislocation absorption [6–8]. This CAI-mediated slip transfer mechanism, combined with the size-confined suppression of mature shear bands, underlies the strength–plasticity synergy of C/A NLs. However, the upper region of the Ashby plot, where ultrahigh strength coexists with large homogeneous strain, remains sparsely populated for nanolaminates, mirroring the challenge faced by other structural materials. When conventional crystalline alloys serve as the constituent layers, C/A NLs can attain a yield strength of ~ 2.5 GPa with nearly 50% homogeneous compressive strain [5]. Replacing them with complex concentrated alloys (CCAs) raises the yield strength to ~ 3.6 GPa, yet the homogeneous strain drops sharply to ~ 15% [9]. Although further optimization can be achieved through layer thickness engineering

* Corresponding authors at: State Key Laboratory of Materials for Advanced Nuclear Energy, Shanghai University, Shanghai 200444, China.
** Corresponding author.
*** Corresponding author.
E-mail addresses: gewuxjtu@xjtu.edu.cn (G. Wu), yandongjia@shu.edu.cn (Y. Jia), ylu1@hku.hk (Y. Lu), bianxilei@shu.edu.cn (X. Bian).
[1] These authors contributed equally to this work.

https://doi.org/10.1016/j.mattod.2026.103450
Received 20 March 2026; Received in revised form 1 July 2026; Accepted 9 July 2026
Available online 24 July 2026
1369-7021/© 2026 Elsevier Ltd. All rights are reserved, including those for text and data mining, AI training, and similar technologies.

[10–12], an intrinsic strategy that simultaneously strengthens the composite and preserves its deformability remains essential.

A promising direction has emerged from recent studies on interstitial alloying. When introduced at appropriate concentrations, interstitial can occupy a state between random solid solution and ceramic precipitation, creating unique nanoscale chemical inhomogeneity in metallic matrices. This manifests as uniformly dispersed covalent bonds or ordered interstitial clusters [13–18]. Such interstitial-mediated chemical heterogeneities generate a rugged energy landscape that impedes the motion of deformation carriers, including dislocations, grain boundaries (GBs), STZs, or shear bands, thereby elevating strength and promoting sustained strain hardening [19]. In heterostructured materials, interstitial atoms with small atomic radii also tend to diffuse under stress gradients and their enrichment in the soft phase effectively strengthens it [20], while diffusion-induced stress relaxation dissipates local stress concentrations [21]. Compared with conventional interstitial strengtheners such as carbon [22], nitrogen [23], and boron [23,24], oxygen offers a particularly attractive balance between strength and ductility [14–16,25,26].

Therefore, inspired by chemical partitioning in C/A NLs [9], we employ oxygen as an alternative modulator, which significantly enhances the chemically adaptive response. Here, we exploit these effects

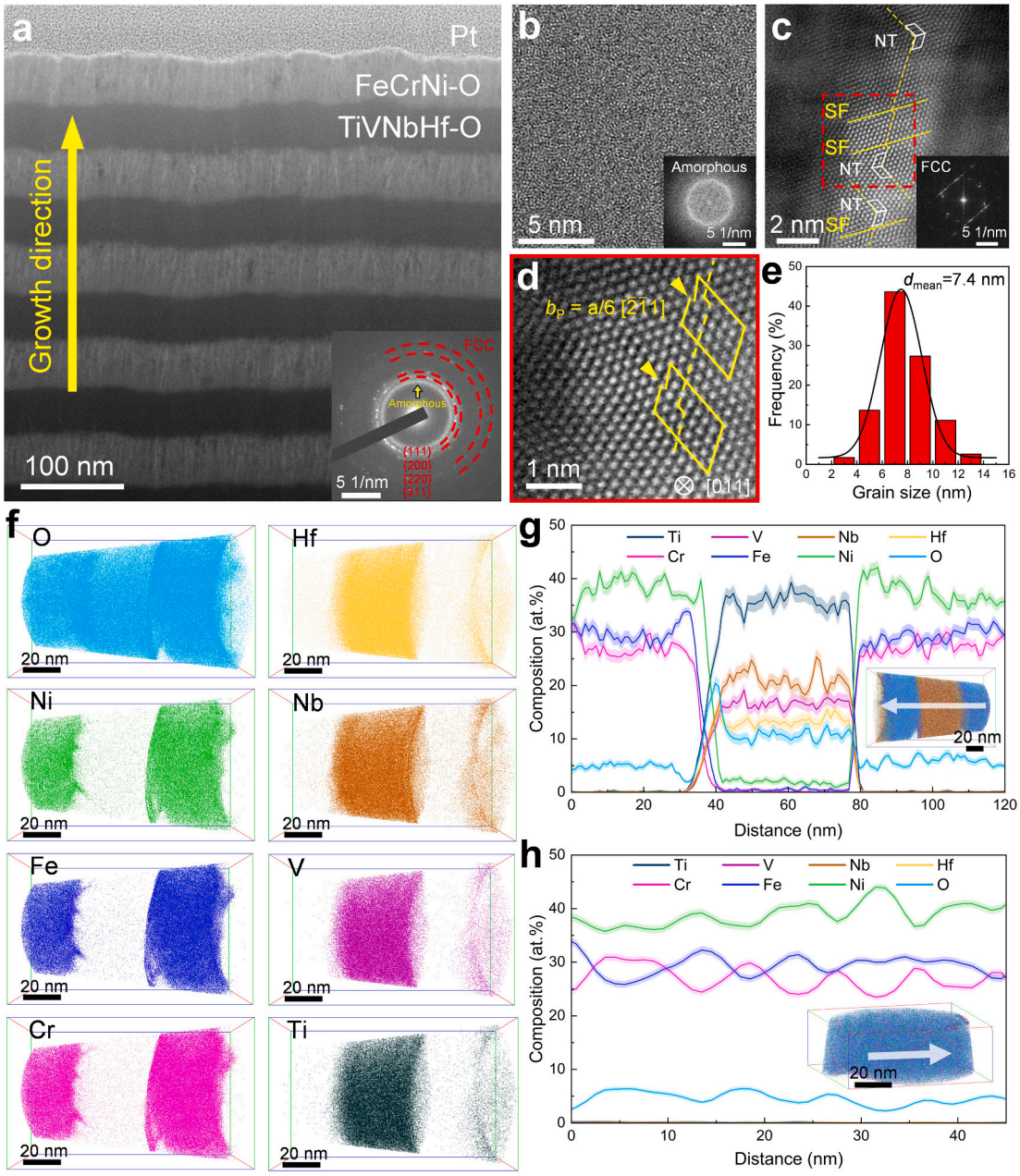


Fig. 1. Microstructure and composition of as-deposited C50/A50 NLs. (**a**) Typical cross-sectional BF-STEM image. SAED pattern (inset) shows a diffuse amorphous ring and sharp rings from the FCC {111}, {200}, {220}, and {311} planes. (**b**) HRTEM image showing the maze-like pattern of the amorphous TiVNbHf-O layer. Inset is the corresponding fast Fourier transform (FFT) image. (**c**) HAADF-STEM image revealing an FCC nanocolumnar grain in the crystalline FeCrNi-O layer, with a high density of SFs and NTs. The corresponding FFT pattern is shown in the inset. (**d**) Magnified HAADF-STEM image of the region marked by the red frame in (**c**) showing two Shockley partial dislocations with *b*p = a/6 [$\overline{2}$1 1] coexisting with SFs. (**e**) Grain size (columnar width) distribution of the nanograins in FeCrNi-O layer. (**f**) Individual 3D elemental mappings. (**g**) 1D compositional profile across the region indicated by the arrow in combined 3D reconstructed APT sample (inset). (**h**) 1D compositional profile across a crystalline layer (marked by an arrow in inset), showing spatial correlation between Cr and O. The light shadows of the curves in (**g**) and (**h**) indicate statistical errors in terms of the standard deviations.

in C/A NLs where both constituent phases accommodate substantial interstitial oxygen. Oxygen is expected to preferentially segregate at CAIs without necessarily causing embrittlement. During deformation, dislocations activated at the CAIs can drag oxygen from the CAIs and the oxygen-rich amorphous layers into the adjacent crystalline layers. Such dynamic partitioning could relieve interfacial stress, enhance intralayer chemical inhomogeneity, and contribute to solid-solution strengthening, thereby reducing stress concentrations and promoting cooperative deformation. Based on this concept, the present work aims to explore oxygen dynamic partitioning as a strategy for designing chemically adaptive NLs that simultaneously achieve high strength and substantial deformability across diverse alloy systems.

Results

Microstructure and chemical analysis of the as-deposited C/A NLs

Three different architectures of oxygen-doped C/A NLs were fabricated with a fixed amorphous layer thickness of 50 nm and varying crystalline layer thicknesses of 25 nm, 50 nm, and 100 nm, designated as C25/A50, C50/A50, and C100/A50, respectively. Corresponding cross-sectional scanning electron microscopy (SEM) images are provided (Fig. S1). The C50/A50 NLs was selected as the model system for detailed structural and chemical analysis. Transmission electron microscopy (TEM) morphology of the C50/A50 NLs reveals a well-defined lamellar microstructure with flat heterogeneous interfaces perpendicular to the growth direction (GD), with individual layer thicknesses of approximately 47 nm and 46 nm (Fig. 1a, Fig. S2). The corresponding selected-area electron diffraction (SAED) pattern shows distinct {111}, {200}, {220}, and {311} peaks, along with a diffuse amorphous ring, consistent with the XRD results (Fig. S3), indicating a FCC/amorphous dual-phase structure without formation of oxides or other secondary phases. The FCC lattice parameter is measured to be 3.65 Å, exhibiting a ~ 1.39% expansion relative to pure FeCrNi (3.60 Å) [27]. A high-resolution TEM (HRTEM) image of the amorphous layer (Fig. 1b), further confirming its structure nature. The high-angle annular dark-field scanning TEM (HAADF-STEM) images of the crystalline layer reveal a nanocolumnar grain structure enriched with stacking faults (SFs) and nanotwins (NTs) (Fig. 1c, Fig. S4). Furthermore, a magnified view of the SF-rich region reveals the presence of Shockley partial dislocations with a Burgers vector of b_P = a/6 [$\bar{2}\bar{1}$ 1] (Fig. 1d). Such a microstructure is typical for metals with low stacking fault energy (SFE) (e.g., 40 mJ/m^2 for FeCrNi [27]) fabricated under the high cooling rate of approximately 10^{10} K s^{-1} in sputter deposition [28,29]. Statistical analysis of the grain size (i.e., the width of the columnar grains) yields an average value of 7.4 nm (Fig. 1e). Atom probe tomography (APT) results reveal that the average compositions of the crystalline and amorphous layers are $Fe_{29.67}Cr_{27.61}Ni_{37.02}O_{5.40}Ti_{0.12}V_{0.02}Nb_{0.11}Hf_{0.05}$ (at.%) and $Ti_{35.91}V_{16.74}Nb_{20.90}Hf_{13.16}O_{10.47}Fe_{0.29}Cr_{0.50}Ni_{2.03}$ (at.%), respectively, indicating atomic intermixing during deposition [3,9] (Fig. 1f). The diffusion of Fe, Cr, and Ni into the amorphous TiVNbHf-O layers is more pronounced than the reverse diffusion of Ti, V, Nb, and Hf into the crystalline FeCrNi-O layers. This asymmetric interdiffusion behavior during deposition can be attributed to the smaller atomic sizes of Fe, Cr, and Ni [9], as well as the higher diffusivity of atoms within the crystalline layers, which contain a high density of defects, compared with the amorphous layers. In addition, oxygen segregation was observed at the CAIs, especially at interfaces where a crystalline layer sits above an amorphous layer (Fig. 1g). Due to the incorporation of oxygen, nanoscale intralaminar chemical inhomogeneity in crystalline layers is clearly observed. The elemental concentration profile perpendicular to the GD (Fig. 1h) shows that Cr and O exhibit correlated spatial variations, i.e., their concentrations increase or decrease simultaneously within the nominal composition [18]. This chemical inhomogeneity likely stems from the strong affinity between oxygen and Cr [32]. For comparison, another alloy system, i.e., crystalline CoCrNi-O/amorphous TiZrNbHf-O NLs with comparable layer thicknesses of ~ 60 nm, were also deposited, and they exhibit similar laminated microstructures and elemental distributions (Fig. S5).

Mechanical properties

Micro-compression tests were conducted to evaluate the mechanical properties of the C/A NLs, monolayer crystalline FeCrNi-O, and amorphous TiVNbHf-O films. The initial micro-pillar morphologies before compression tests are provided (Fig. S6). Each compression test was repeated three times. Representative engineering stress–strain curves and the corresponding post-compression morphologies of the micro-pillars are presented (Fig. 2a-b). Notably, even the monolayer crystalline FeCrNi-O sample exhibits fine, dense serrations in the stress–strain curve, similar to those observed in the C/A NLs (Fig. 2a). In contrast to the large stress drops typically associated with shear banding behavior [33,34], these serrations are likely resulted from dislocation motion and the activation of slip systems within the crystalline layers during plastic deformation, as observed in previous studies [3,35,36]. The amorphous TiVNbHf-O alloy exhibits the highest yield strength (σ_y) of 5.02 ± 0.06 GPa among the tested materials, but undergoes inhomogeneous deformation characterized by extensive shear bands (Fig. 2b$_1$). In contrast, the monolayer FeCrNi-O alloy, which has the lowest yield strength (2.83 ± 0.13 GPa), deforms smoothly without shear bands (Fig. 2b$_2$), indicating a superior capacity for uniform plastic deformation [37]. The yield strength of the C/A NLs falls between those of the amorphous TiVNbHf-O and nanocrystalline FeCrNi-O alloys. To benchmark the mechanical performance, the yield strength of the C/A NLs was compared with the rule of mixtures (ROM) prediction. A positive deviation is observed, indicating properties superior to a simple average of the constituents (Fig. S7), which suggests a marked effect of interfaces on the mechanical properties [8,38,39]. Specifically, the C25/A50 NLs exhibit a yield strength of 4.30 ± 0.05 GPa. Although no obvious stress drops are observed in the stress–strain curve, the compressed pillar shows inhomogeneous deformation (Fig. 2b$_3$), manifested as lateral deflection rather than global compression, with *trans*-layer shear band observed at the bent region [6,40]. When the crystalline layer thickness increases to 100 nm (C100/A50 NLs), the yield strength decreases to 3.63 ± 0.13 GPa due to the increased volume fraction of the crystalline phase, while the capacity for uniform deformation is retained (Fig. 2b$_4$). In stark contrast, the C50/A50 NLs, despite having a larger crystalline phase fraction than C25/A50, achieve the highest yield strength (4.37 ± 0.12 GPa) among the NLs while still deforming uniformly without visible shear bands (Fig. 2b$_5$-b$_6$; reasons for the absence of shear bands are detailed in Supplementary Text S1). Therefore, among all the thin films investigated, the C50/A50 NLs demonstrate the most superior mechanical properties, characterized by the highest yield strength (4.37 GPa) and a considerable uniform deformation capability (over 50%). The corresponding true stress–strain curves are displayed in Fig. S8, demonstrating strain hardening behavior of the C/A NLs. We also performed in-situ TEM tensile testing to investigate the tensile behavior of C50/A50 NLs at room temperature (Fig. 2c). The TEM lamella, with a thickness of approximately 86 nm, contains four FeCrNi-O/TiVNbHf-O structural units along the GD, thus representing the average mechanical response of the C/A NLs. The material exhibits obvious strain hardening, with a yield strength (σ_y) of 1.07 GPa and a fracture strength (σ_f) of 1.74 GPa. These outstanding properties are also replicated in the crystalline CoCrNi-O/amorphous TiZrNbHf-O system even with larger layer thicknesses (~60 nm), outperforming the oxygen-free counterpart system (crystalline CoCrNi/amorphous TiZrNbHf NLs with 18/12 nm layer thicknesses) reported previously [9] (Fig. S9). Therefore, this oxygen engineering strategy proves fundamentally versatility beyond specific compositions, establishing a universal paradigm for designing ultra-strong and ductile nanolayered materials. We anticipate widespread technological applications leveraging these oxygen-tailored C/A

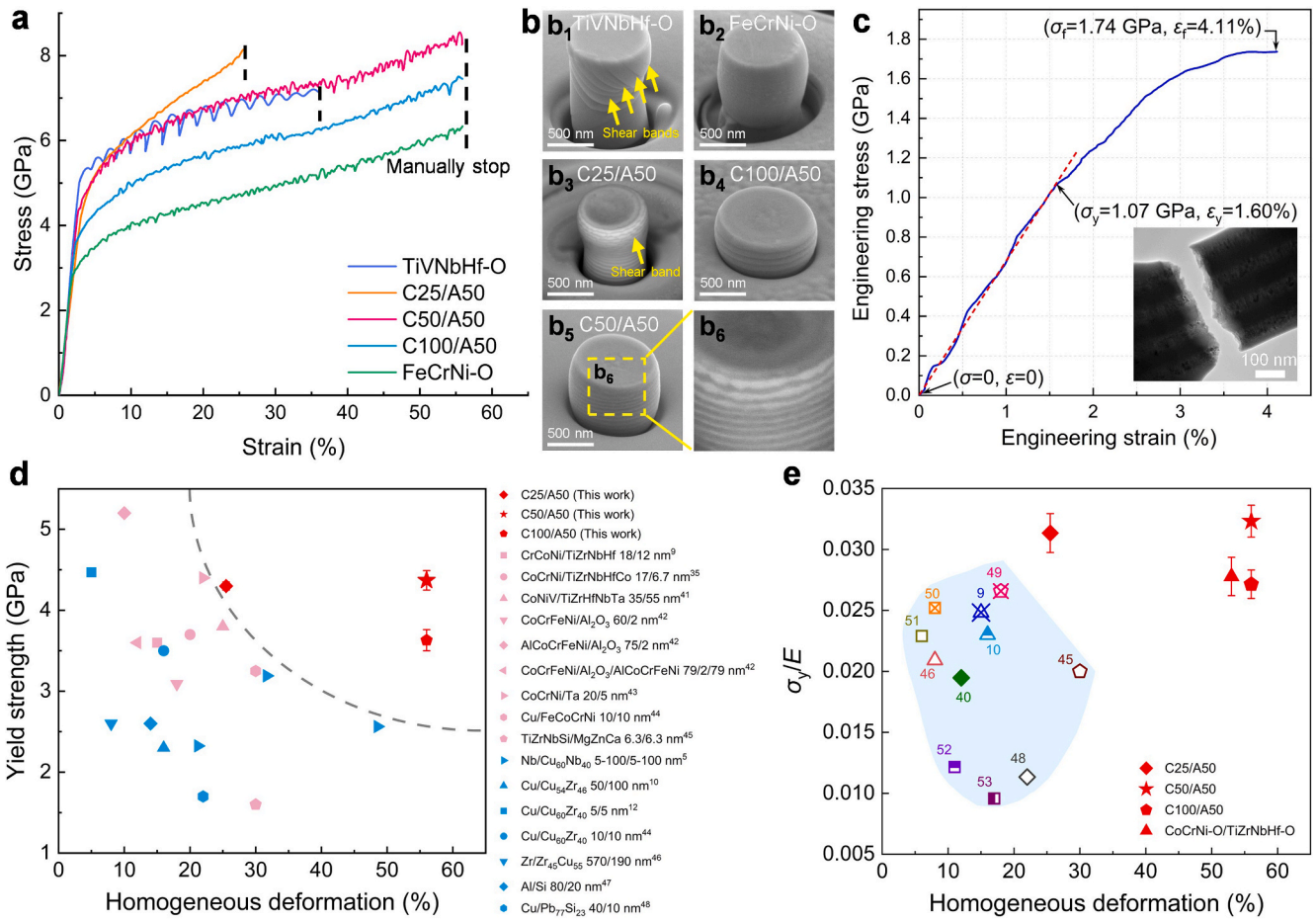


Fig. 2. Improved mechanical properties of the NLs. (a) Representative compressive engineering stress–strain curves of the C/A NLs and monolayer films. (b) SEM images of the micro-pillars after deformation. Magnified image reveals no presence of shear bands in the C50/A50 sample. (c) Tensile engineering stress–strain curve showing ~ 4.11% elongation to failure. The insert shows the fracture morphology. (d) Yield strength vs. homogeneous plastic strain of the FeCrNi-O/TiVNbHf-O NLs, in comparison with previous findings of CCA-based NLs (pink icons) [9,35,41–45] and conventional C/A NLs (blue icons) [5,10,12,44,46–48] tested via micro-compression. (e) Normalized strength (yield strength/elastic modulus, σ_y/E) vs. homogeneous deformation strain of the current studied NLs (C25/A50, C50/A50, C100/A50, and CoCrNi-O/TiZrNbHf-O), in comparison with the literature reported nanolayered materials [9,10,40,45,46,48–53]. Error bars represent standard deviations.

nanolaminates, particularly in extreme mechanical environments requiring supreme wear resistance such as next-generation cutting tools.

The relationship between yield strength and homogeneous plastic deformation of the C/A NLs is summarized (Fig. 2d), and also compared with the findings previously reported for CCA NLs [9,35,41–45] and conventional C/A NLs [5,10,12,44,46–48]. Obviously, our C/A NLs placed in the upper right corner, particularly the C50/A50 NLs, exhibit a superior strength-deformability synergy compared to other NLs systems. This underscores the effectiveness of oxygen–mediated nanolayered design in overcoming the traditional strength–plasticity trade-off in CCA–based composite materials. More intriguingly, the normalized strength, σ_y/E (where E represents the elastic modulus, Fig. S10), of the present FeCrNi-O/TiVNbHf-O and CoCrNi-O/TiZrNbHf-O C/A NLs reach nearly E/30, substantially surpassing most reported nanolayered materials [9,10,40,45,46,48–53] (Fig. 2e) and approaches the theoretical strength ($\sim E/10$) [54], further demonstrating the synergistic strengthening effect achieved in such nanolayered structures via oxygen engineering.

Evolution of microstructure and chemical inhomogeneity during deformation

Cross-sectional TEM analysis was conducted on the C50/A50 micro-pillars compressed to an overall engineering strain of 56% to elucidate the underlying deformation mechanisms (Fig. 3). In the central region of the sample, the individual layer thickness was reduced to approximately 16 nm, corresponding to a local strain of ~ 70%. Even under such severe deformation, no shear bands were observed throughout the structure, and the amorphous/FCC dual-phase structure remains intact, as confirmed by the inset SAED patterns (Fig. 3a). After deformation, a large proportion of the original nanocolumnar crystals in the FeCrNi-O layers transforms into spherical units with an average diameter of ~ 5.7 nm (Fig. 3b, Fig. S11), without evidence of grain growth driven by GB instability [55]. The TiVNbHf-O layers retain a homogeneous amorphous structure with no evidence of crystallization or amorphous phase separation (Fig. 3c). Fig. 3d shows the presence of NT, SF and coexisting Shockley partial dislocations (b_P = a/6 [$\bar{2}11$]), within the crystalline layer near the CAI after large deformation, confirming that partial dislocations persistently mediate plastic deformation throughout the process.

High-magnification HAADF-STEM imaging combined with EELS was employed to characterize compositional evolution in the deformed C50/A50 NLs (Fig. 3e). The contrast in the HAADF-STEM image largely depends on the atomic number, whereby the brighter areas correspond to regions enriched in heavier atoms [56]. To improve the energy resolution of EELS, the maximum energy loss of the spectrum was set to be 1100 eV (Fig. S12) and only the Ti signal was utilized to represent the TiVNbHf-O layers. Unlike the sharp CAIs in the as-deposited film, the

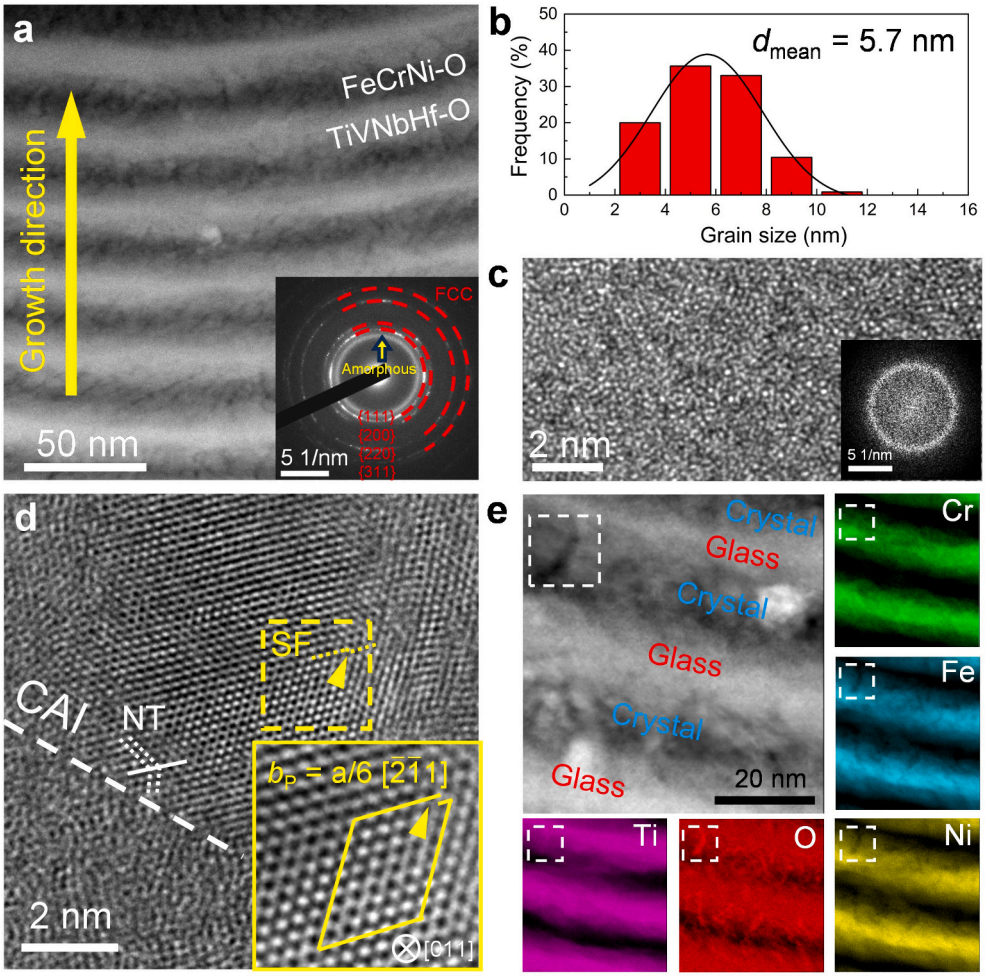


Fig. 3. Microstructure and composition of the C50/A50 NLs after compression. (**a**) HAADF-STEM image of the post-deformed micro-pillar with ~ 56% plastic strain. The inset shows the corresponding SAED pattern, revealing the constant amorphous/FCC dual-phase structure. (**b**) Grain size distribution histogram. (**c**) HRTEM image of the TiVNbHf-O layer, exhibiting typical amorphous characteristics. The inset displays the corresponding FFT pattern. (**d**) HRTEM image acquired near the CAI, with a SF and a NT identified within the crystalline layer. The inset presents a magnified view of the yellow-boxed region, revealing a Shockley partial dislocation with a Burgers vector of $b_P = a/6\ [\bar{2}\bar{1}1]$ associated with the SF. (**e**) High-magnification cross-sectional HAADF-STEM image and the corresponding EELS mapping of O, Ti, Fe, Cr and Ni in the deformed sample. The white dashed rectangles indicate regions with distinct elemental distributions.

interfacial chemical profile becomes blurred after deformation, suggesting interlayer element mixing. Compared to as-deposited samples, chemical fluctuations within the crystalline layers, including distinct (Cr, O)-enriched and (Fe, Ni)-enriched regions, become more pronounced in the compressed samples. Notably, chemical fluctuations are spatially uniform throughout the crystalline layers and show no correlation with structural features such as GBs or intra-grain defects (e.g., NTs and SFs), as confirmed by correlating EELS mappings with HAADF-STEM images (Fig. 3e). Such nanoscale chemical inhomogeneity can significantly enhance the flow stress and strain hardening of nanocrystalline layers through interactions with dislocations and GBs [57,58]. Conversely, EELS mappings of Ti and O reveal that the amorphous layers maintain a chemically homogeneous distribution before and after deformation, with no formation of oxygen clusters despite with higher oxygen content (Fig. 3e). This behavior is further confirmed by binomial frequency distribution analysis based on APT, in which the elemental concentration distributions in the amorphous layers closely match the reference binomial random distributions both before and after deformation, whereas those in the crystalline layers exhibit significant deviations (Fig. S13). This distinct elemental distribution behavior between crystalline and amorphous layers primarily arises from differences in interatomic affinity (particularly for oxygen) and atomic size. As summarized in Table S1, oxygen exhibits a substantially larger electronegativity difference with Cr than with Fe or Ni. Moreover, both Cr and O are relatively small atoms, which facilitates their strong interactions and clustering. In contrast, oxygen shows comparable electronegativity differences with Ti, V, and Nb. Although a notable difference exists with Hf, its long-range diffusion is suppressed by its low concentration and large atomic size, thereby promoting a homogeneous distribution in the amorphous layer.

The specific elemental composition within the crystalline and amorphous layers has changed after deformation, with average layer compositions of $Fe_{29.25}Cr_{27.68}Ni_{35.89}O_{6.95}Ti_{0.11}V_{0.02}Nb_{0.07}Hf_{0.03}$ (at.%) and $Ti_{36.45}V_{17.04}Nb_{19.96}Hf_{11.67}O_{9.88}Fe_{0.91}Cr_{0.74}Ni_{3.35}$ (at.%), respectively (Fig. 4a). Line scans across the deformed sample reveal the presence of element mixing layers, with thicknesses reaching up to 8 nm in severely deformed regions, nearly half the thickness of the adjacent crystalline or amorphous layers. Additionally, the unexpected reduction of oxygen enrichment at the CAIs after deformation further indicates that the interfaces dynamically participate in the deformation process, serving not merely as sinks for defects but also as sources, from which oxygen is transported away by mobile defects [8]. Interface identification was based on Hf content, which exhibits minimal diffusion. Regions with Hf > 10.00 at.% were defined as amorphous layers, those with Hf < 0.10 at.% as crystalline layers, and regions with intermediate Hf content were classified as mixed layers (Fig. 4b). Magnified views of the

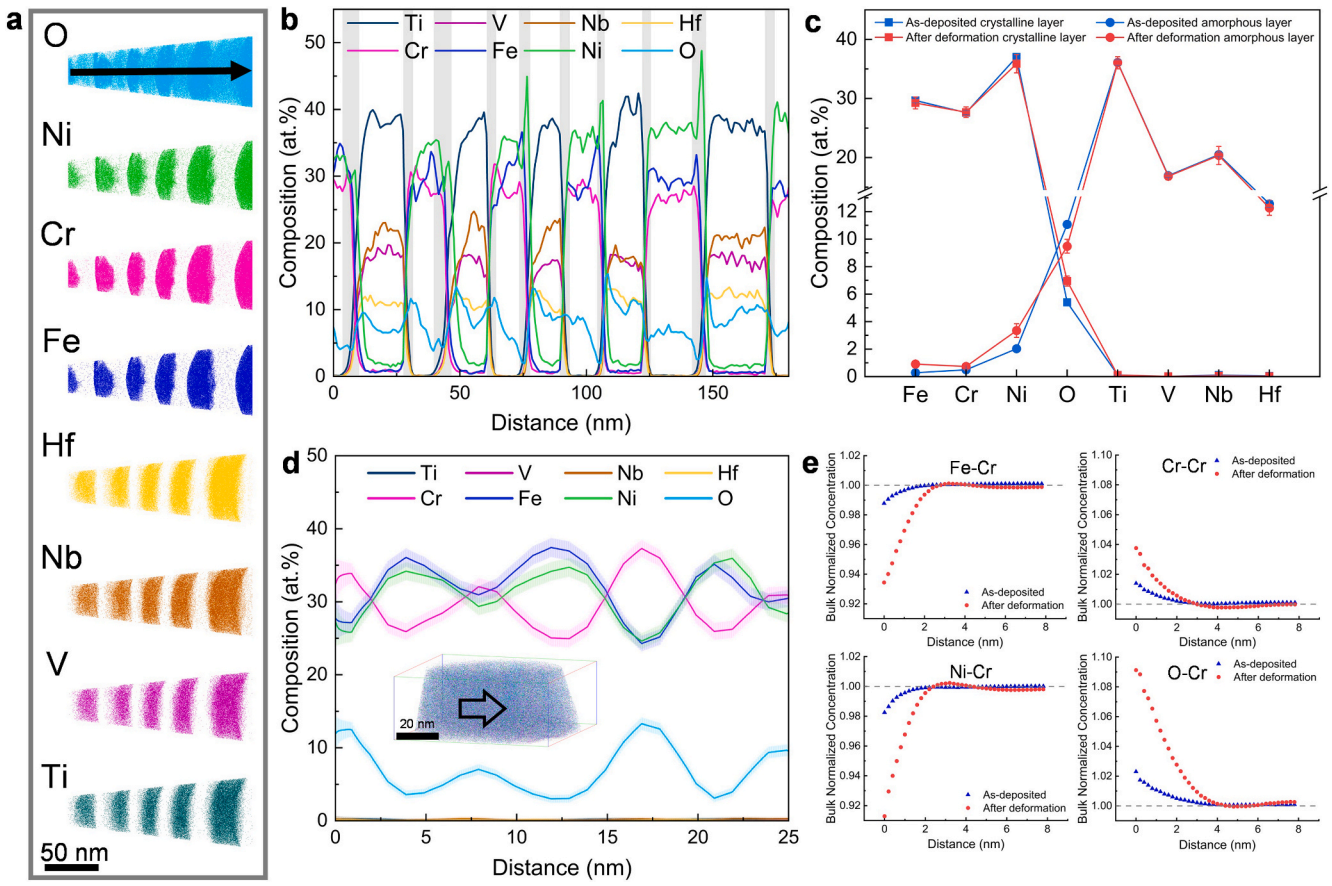


Fig. 4. Quantification of interlayer diffusion and chemical evolution of C50/A50 NLs during deformation. (**a**) Individual 3D elemental maps of C50/A50 NLs. (**b**) 1D compositional profile across APT sample (marked by an arrow in (**a**)). The intermixed layers were labeled by grey shadows. (**c**) Specific elemental contents in the crystalline and amorphous layers before and after deformation. To accentuate the distinct diffusion behaviors, the *y*-axis is broken from 13.1 to 14.5 at.%, clearly contrasting the pronounced outward diffusion of Fe, Cr, Ni, and O from the crystalline layer against the minimal counter-diffusion of Ti, V, Nb, and Hf. Error bars represent standard deviations. (**d**) 1D compositional profile across a combined 3D reconstructed crystalline layer (marked by an arrow in inset). The light shadows of the curves indicate statistical errors in terms of the standard deviations. (**e**) Calculated Cr RDFs from the APT data with Fe, Cr, Ni and O as the center atoms, respectively, for the C50/A50 NLs before and after deformation. Note that the RDFs are normalized by the averaged composition for the APT-analyzed volume. A value > 1 indicates enrichment, while a value < 1 indicates depletion of Cr around the central atoms.

element mixing layer before and after deformation are provided in Fig. S14. The observed interdiffusion is primarily attributed to Ni and O,

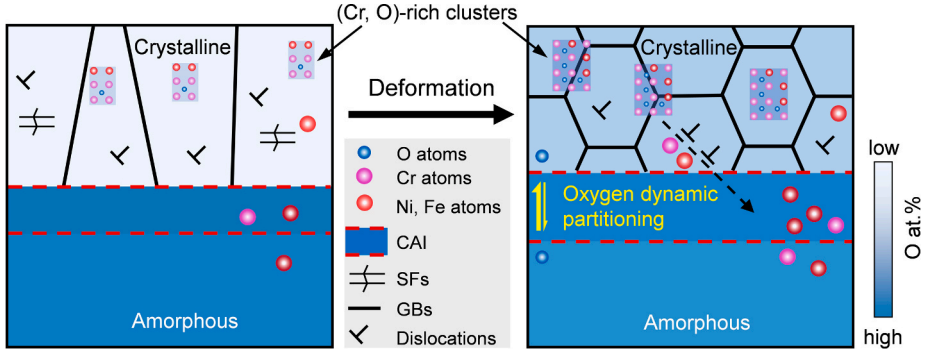


Fig. 5. Schematic illustration of the structure evolution during plastic deformation in the FeCrNi-O/TiVNbHf-O C/A NLs. In the as-deposited C/A NLs (left panel), the crystalline layers contain SFs and slight compositional fluctuations, specifically (Cr, O)-rich clusters. The average oxygen concentration in the amorphous layers is higher than that in the crystalline layers, with significantly enrichment at the CAIs. Atoms from the crystalline phase diffuse into the amorphous phase due to their higher mobility under deposition conditions. Upon deformation (right panel), the moving dislocations cut through the columnar grains and refine them. These dislocations drag Fe, Cr, and Ni atoms, leading to their continuous diffusion from the crystalline layers to the amorphous layers, with more pronounced in diffusion of Fe and Ni. Simultaneously, oxygen atoms, driven by the concentration gradient and assisted by stress, diffuse from the amorphous layers and CAIs into the crystalline layers. After deformation, the average oxygen concentration is lowered in the amorphous layers and increased in the crystalline layers, accompanied by weakened enrichment at the CAIs. Such oxygen dynamic partitioning amplifies compositional fluctuations (i.e., the growth of (Cr, O)-rich clusters) and drives the progressive hardening of the softer crystalline layers and promotes effective stress dissipation at the CAIs via stress relaxion, collectively enabling synergistic co-deformation of the two phases.

which possess the smallest atomic sizes. In the amorphous layer, the Ni content increased from 2.03 ± 0.1 at.% to 3.35 ± 0.5 at.%, while the O content decreased by approximately 1.59 at.%. Correspondingly, the O content in the crystalline layer increased by about 1.55 at.% (Fig. 4c). The amplified chemical inhomogeneity in the crystalline layers after deformation was further quantitatively demonstrated by APT analysis. Line scan profiles reveal strongly correlated spatial fluctuations of Cr and O, characterized by synchronous concentration variations exceeding ± 3.44 at.% from the nominal composition (Fig. 4d). The radial distribution functions (RDFs) in Fig. 4e show that after deformation, Cr becomes markedly enriched around central Cr and O atoms (normalized concentration > 1), alongside a depletion around central Fe and Ni atoms (normalized concentration < 1), compared to the pre-deformation state. This statistically significant anti-correlation provides strong evidence for the formation of (Cr, O) clusters in the crystalline layers during deformation.

Discussion

We employ a schematic illustration (Fig. 5) to describe the deformation-induced oxygen dynamic partitioning mechanism. In the as-deposited state, the crystalline and amorphous layers possess compositions of Fe-Cr-Ni-O and Ti-V-Nb-Hf-Fe-Cr-Ni-O, with oxygen contents of 5.40 at.% and 10.47 at.%, respectively. The incorporation of oxygen already induces nanoscale chemical inhomogeneities in the crystalline phase, forming (Cr, O)-rich clusters that act as local barriers to dislocation motion [14,19]. In the amorphous layers, directional oxygen-metal (O-M) covalent bonds are uniformly embedded within the metallic matrix, substantially strengthening the amorphous phase, as evidenced by the pure TiVNbHf-O amorphous alloy which exhibits a compressive strength reaching 5 GPa [13]. Although pronounced oxygen segregation occurs at the CAIs, no oxides are formed. Consequently, the O-M covalent bonds at the interfaces also contribute to enhanced interfacial bonding [18,25]. The post-deformation depletion of oxygen at the CAIs further indicates that these oxygen-strengthened interfaces dynamically participate in the co-deformation of the two phases.

Upon deformation, dislocations nucleate preferentially at the CAIs and glide through the crystalline layers [8], where their motion is strongly influenced by the heterogeneous chemical environment. When these dislocations reach the opposite interface, they are either absorbed or transmitted into the amorphous phase [7,8], thereby providing fast diffusion channels along which crystalline-phase constituents, especially Ni, concurrently diffuse from the crystalline layers into the amorphous phase driven by the chemical potential gradient [6,9]. Meanwhile, interface-mediated dislocation nucleation can simultaneously transfer atoms such as oxygen from the amorphous phase and CAIs into the crystalline layers [6,29]. Unlike the transport of Ni, the diffusion of O from the amorphous phase and CAIs into the crystalline layers is primarily dragged by dislocations, proceeding uphill against the chemical potential gradient due to its greater affinity for the amorphous-phase constituents [59,60]. Although the energy barrier between the crystalline and amorphous layers can reach approximately 276.45 kJ/mol, the 5–8 nm thick CAI acts as a diffusional step that smooths the gradient over a finite distance, such that over one Burgers vector ($b_P = 1.49$ Å) the barrier is reduced to only about 8.24 kJ/mol. This value is substantially lower than the interaction energy E_I (−53.64 kJ/mol, derived from the Cottrell–Bilby model [61]) between oxygen atoms and the stress field of an edge dislocation, which not only enables strong oxygen segregation but also facilitates the dragging of oxygen atoms from the amorphous layers into the crystalline layers during deformation. Thus, this dislocation-assisted atomic transport establishes the CAIs as active channels for mass exchange, leading to progressive interfacial broadening, chemical intermixing, and stress relaxation [21]. Further details on the dislocation dragging mechanism are provided in Supplementary Text S2.

As a result, the elemental distribution evolves significantly during deformation: Ni content in the amorphous layers increases (from 2.03 to 3.35 at.%), while oxygen content decreases (from 10.47 to 9.88 at.%), whereas the crystalline layers experience a pronounced oxygen enrichment (from 5.40 to 6.95 at.%). This redistribution reflects the continuous interaction between dislocations and interfaces, which drives chemical equilibration across the CAIs. The elevated Ni content in the amorphous layers increases the negative mixing enthalpy, thereby stabilizing the amorphous structure [9]. Meanwhile, oxygen enrichment in the crystalline layers induces lattice distortion and exerts a strong pinning effect on dislocations. According to the Fleischer-Friedel strong-pinning model, the oxygen content increase from 5.40 to 6.95 at.% in the FeCrNi layers raises the critical resolved shear stress (CRSS) by approximately 230 MPa [62,63]. Accounting for a Taylor factor of 2–3.06, this corresponds to an increment in the yield strength of the crystalline layers of 460–704 MPa (see Supplementary Text S3 for details). Beyond this solid-solution strengthening, the chemical bonding between oxygen and the matrix elements, together with the amplified chemical fluctuations, creates a rugged energy landscape for dislocation motion, further enhancing both the strength and the work-hardening capacity of the crystalline layers [15]. In addition, the increased oxygen segregation at GBs stabilizes the nanocrystals and suppresses GB activity-induced softening [18]. Consequently, dislocations experience frequent pinning, reconfiguration, and trapping at both lattice defects and interfaces, leading to reduced mobility and sustained strain hardening.

At the same time, the evolving interface chemistry improves the mechanical compatibility between the crystalline and amorphous phases. The reduction in modulus and strength mismatch alleviates stress concentrations at the CAIs, suppresses interfacial failure, and promotes efficient load transfer [45,64]. Moreover, the CAIs function as continuous sources and sinks for dislocations, regulating their density and preventing excessive accumulation within the crystalline layers [8]. This dynamic balance between dislocation emission, absorption, and interface-mediated transport ensures stable and distributed plastic deformation [9,65].

In addition, the strong coupling between dislocation activity and the amorphous phase deformation suppresses shear band formation. The absorption and transmission of dislocations at the CAIs promote the activation of distributed STZ in the amorphous layers, rather than localized shear bands [8]. As a result, the high-strength amorphous phase, the continuously hardening crystalline phase, and the chemically and structurally evolving interfaces act cooperatively to enable homogeneous plastic deformation.

In summary, the exceptional mechanical performance of the C50/A50 nanolaminates originates from the interface-governed interaction between dislocations and chemical partitioning. The CAIs mediate dislocation dynamics, drive atomic redistribution, and reduce mechanical incompatibility between phases, thereby enabling coordinated deformation. This synergistic mechanism underpins the simultaneous achievement of ultrahigh strength and large uniform deformability in these C/A NLs.

Conclusions

In summary, we demonstrate a design strategy that moves beyond the conventional static architecture of C/A NLs into chemically adaptive systems through oxygen dynamic partitioning. By harnessing interstitial oxygen as an in situ chemical modulator, the FeCrNi-O/TiVNbHf-O system undergoes continuous oxygen redistribution from the amorphous to the crystalline layers during deformation. This dynamic chemical evolution progressively strengthens the crystalline phase and narrows the property gap between the two constituents, enabling coordinated deformation across the interfaces. The resulting C/A NLs exhibit excellent mechanical properties with ultra-high strength and large plastic strain, outperforming state-of-the-art high-performance NLs. Especially, the C50/A50 NLs achieve an exceptional combination of

near-theoretical yield strength (4.37 GPa, ~E/30) and extensive uniform deformability (exceeding 50%) under compression, with no signs of shear localization. Beyond the specific system studied, this approach offers a versatile design route that leverages dynamic chemical effects to create nanolayered materials capable of adapting under mechanical loading. This work also provides impetus for their potential applications in coatings, micro-electromechanical systems, and flexible devices.

Methods

Materials preparation

The FeCrNi-O/TiVNbHf-O and CoCrNi-O/TiZrNbHf-O C/A multilayer films were deposited on Si (100) substrates by direct current magnetron sputtering at room temperature. $(FeCrNi)_{98}O_2$ (at.%), $Ti_{38}V_{15}Nb_{23}Hf_{21}O_3$ (at.%), $(CoCrNi)_{99}O_1$ (at.%), and $Ti_{30}Zr_{22}Nb_{25}Hf_{20}O_3$ (at.%) alloy targets were used for alternating sputtering. The oxygen content in the alloy targets was measured using a LECO ONH836 analyzer. During sputtering, the power of the two targets was switched between on and off for 30 s. The background vacuum was 8×10^{-4} Pa and the Ar working pressure was 0.3 Pa. The distance between substrates and targets was 120 mm and the sputtering power was 60 W. During sputtering, the substrates were rotated at a rate of 10 r/min without applying bias voltage. For FeCrNi-O/TiVNbHf-O NLs, the thickness of the crystalline FeCrNi-O layer was varied between 25, 50, and 100 nm, and the thickness of the amorphous TiVNbHf-O layer was fixed at 50 nm. Accordingly, the samples are termed as C25/A50, C50/A50 and C100/A50, respectively. For CoCrNi-O/TiZrNbHf-O NLs, the thickness of CoCrNi-O and TiZrNbHf-O are 57 nm and 63 nm, respectively. For comparison, FeCrNi-O, CoCrNi-O, TiVNbHf-O, and TiZrNbHf-O monolayer films were prepared on the same substrates using identical conditions. The total thickness of all deposited films was 1.4–1.8 μm.

Structural characterization

To examine the phase structure and crystallographic texture of the films, X-ray diffraction (XRD) was performed at room temperature using a Rigaku Smartlab 9 kW device with Cu-Kα radiation to examine the microstructure. The incidence angle was 0.8° and the scan speed was 5°/min. Microstructures and phase analysis of the films were examined by transmission electron microscopy (TEM, JEOL F200 microscope operated at 200 kV) and spherical aberration-corrected STEM (JEOL JEM-ARM300F, operated at 300 kV) equipped with EELS. The TEM samples were prepared using a focused ion beam (FIB) workstation (Helios NanoLab 600i). The final milling was performed at 2 kV and 23 pA, ensuring minimal FIB-induced damage.

Elemental composition analysis at the atomic scale

Atom probe tomography (APT) (CAMECA LEAP 4000X HR) was employed to detail the elemental compositions of the NLs. The specimens were analyzed under laser mode at a temperature of 50 K, with a pulse energy of 60 pJ, an evaporation detection rate of 1% atom per pulse, and a pulse rate of 200 kHz. Data analysis and three-dimensional (3D) atom map reconstruction were performed using the CAMECA IVAS 3.8 software. The APT samples were fabricated using annular milling in a FIB workstation, wherein the current was progressively reduced as the specimen diameter decreased. The final parameters used for cleaning were 2 kV/23 pA.

Mechanical property characterization

Nanoindentation tests were performed using a Berkovich diamond indenter with a tip radius of ~ 100 nm on a commercial nanoindentation system (Hysitron TI 980 TriboIndenter, Bruker) at room temperature. The tip area function for the Berkovich tip was carefully calibrated on a fused silica standard sample before running the tests. The thermal drift was maintained at 0.05 nm/s for all experiments. The experiments were carried out using continuous stiffness measurement (CSM) in load-controlled mode with a peak load of 8 mN at an applied strain rate of 0.1 s^{-1}. Nine indents were performed on each sample to obtain the average hardness (H) and reduced modulus (E_r).

The compressive performance of the films was measured using a Hysitron TI 980 TriboIndenter (Bruker) by employing a flat diamond tip with a diameter of 10 μm at room temperature. The tests were conducted in feedback-enabled displacement-controlled mode at a specified nominal strain rate of 3×10^{-3} s^{-1}. To enhance the reliability of the experimental results, three repeated tests were conducted for each diameter micro-pillars under the same conditions. Micro-pillar samples with a diameter of ~ 600 nm and an aspect ratio of ~ 2 were prepared by dual-beam focused ion beam/scanning electron microscopy (FIB/SEM, Helios NanoLab 600i). The taper angles were smaller than 2.5°, minimizing the impact of pillar geometry. The stress was calculated by: $4P/[\pi(D_0 + 2d\tan\theta)^2]$ [66], where P is the load, D_0 is the tip diameter, d is the tip displacement, and θ is the taper angle. The strain was calculated from the ratio of the recorded displacement data to the height of the unloaded pillars after taking into account the machine and substrate compliance [67]. The morphology of the micro-pillars prior to and after the deformation was observed by secondary electron imaging mode and backscattered electron imaging mode of a SEM (ZEISS Gemini 300).

In-situ TEM tension

The tensile specimen was prepared using focused ion beam (FIB) milling with a Helios 5 Plasma FIB (PFIB, Thermo Fisher Scientific), which operates with xenon ions. A lamella was extracted from the multilayer system using ion beam currents ranging from 15 nA to 1 nA at 30 kV, and was transferred onto a push-to-pull MEMS chip (Hysitron, Bruker) using FIB-assisted chemical vapor deposition of tungsten. Final thinning and polishing of the specimen were conducted directly on the MEMS chip, with progressively lower ion beam currents from 300 pA at 30 kV down to 20 pA at 2 kV, to minimize FIB-induced amorphization of the specimen. The final sample thickness was 86 nm. The specimen was shaped into a dog-bone geometry using a 10 pA beam at 30 kV. Special care was taken to limit ion beam exposure and reduce damage from irradiation.

In-situ tensile testing was carried out on a JEOL JEM 2200FS TEM operating at 200 kV. The microscope is equipped with a 4 k CMOS camera (TVIPS XF416) for high-resolution imaging. Mechanical testing was performed using a Hysitron PI95 nano indenter (Hysitron, Bruker), allowing simultaneous recording of load and displacement. The test was conducted in displacement-controlled mode at a rate of 1.0 $nm{\cdot}s^{-1}$, corresponding to a nominal strain rate of approximately 1×10^{-3} s^{-1}.

CRediT authorship contribution statement

Xiaolong Yu: Writing – original draft, Visualization, Validation, Software, Methodology, Investigation, Formal analysis, Data curation. **Guodong Sun:** Writing – original draft, Visualization, Validation, Software, Methodology, Investigation. **Daniel Şopu:** Writing – review & editing, Methodology. **Lukas Schretter:** Methodology, Investigation. **Christoph Gammer:** Methodology, Investigation, Data curation. **Yifeng Li:** Visualization, Methodology, Investigation, Data curation. **Ge Wu:** Writing – review & editing, Visualization, Validation, Methodology, Funding acquisition. **Chang Liu:** Methodology. **Yandong Jia:** Methodology. **Jürgen Eckert:** Writing – review & editing, Methodology. **Yong Yang:** Visualization, Validation, Formal analysis. **Yang Lu:** Writing – review & editing, Visualization, Validation. **Gang Wang:** Writing – review & editing, Supervision, Resources, Project administration, Funding acquisition, Conceptualization. **Xilei Bian:** Writing – review & editing, Visualization, Validation, Supervision, Methodology, Funding

acquisition, Data curation, Conceptualization.

Declaration of competing interest

The authors declare that they have no known competing financial interests or personal relationships that could have appeared to influence the work reported in this paper.

Acknowledgments

This work was supported by the National Natural Science Foundation of China (Grant Nos. 52171159, 52271114 and 52361165617), the Natural Science Foundation of Shanghai (22ZR1422500), the Shanghai Science and Technology Innovation Action Plan (No. 24CL2901500), the Technology Plan Program of Shanghai Municipal Commission of Science and Technology (No. 25CL2902300), the Shanghai Municipal Explorer Program (No. 25TS1401900), and the Austrian Science Fund (FWF) 10.55776/Y1236, 10.55776/PIN7480424. We thank Jie Li, Jianchao Peng and Hui Li at Shanghai University for technical supports.

Appendix A. Supplementary data

Supplementary data to this article can be found online at https://doi.org/10.1016/j.mattod.2026.103450.

Data availability

All data supporting the findings of this study are available within the article and its Supplementary Information or from the corresponding authors upon request.

References

[1] M.A. Meyers, et al., Prog. Mater Sci. 51 (2006) 427–556.
[2] W.H. Wang, et al., Mater. Sci. Eng. R. Rep. 44 (2004) 45–89.
[3] Y. Wang, et al., Proc. Natl. Acad. Sci. U. S. A. 104 (2007) 11155–11160.
[4] T.G. Nieh, et al., Scr. Mater. 41 (1999) 929–935.
[5] F. Qin, et al., Int. J. Plast (2025) 104294.
[6] W. Guo, et al., Phys. Rev. Lett. 113 (2014) 035501.
[7] T. Phan, et al., Acta Mater. 189 (2020) 10–24.
[8] Q. Xu, et al., Acta Mater. 237 (2022) 118191.
[9] G. Wu, et al., Mater. Today 51 (2021) 6–14.
[10] W. Guo, et al., Acta Mater. 80 (2014) 94–106.
[11] Y.Q. Wang, et al., Acta Mater. 95 (2015) 132–144.
[12] J.Y. Zhang, et al., Acta Mater. 60 (2012) 7183–7196.
[13] Z. Cai, et al., Nature 652 (2026) 1–7.
[14] T. Song, et al., Nature 618 (2023) 63–68.
[15] Z. Lei, et al., Nature 563 (2018) 546–550.
[16] F. Li, et al., Nat. Mater. 23 (2024) 52–57.
[17] L. Shao, et al., Nat. Commun. 15 (2024) 4159.
[18] X.L. Yu, et al., Nat. Commun. 16 (2025) 10602.
[19] E. Ma, C. Liu, Prog. Mater Sci. 143 (2024) 101252.
[20] B. Gao et al., Sci. Adv. 6 (2020) eaba8169.
[21] D.L. Beke, et al., Mater. Sci. Eng. A 387–389 (2004) 4–10.
[22] Z. Wang, et al., Acta Mater. 120 (2016) 228–239.
[23] Y. Chen, et al., Acta Mater. 277 (2024) 120214.
[24] A. Kretschmer, et al., Acta Mater. 299 (2025) 121413.
[25] D. Zhao, et al., Mater. Today 85 (2025) 17–26.
[26] Q. Jia, et al., Acta Mater. 232 (2022) 117934.
[27] M. Schneider, G. Laplanche, Acta Mater. 204 (2021) 116470.
[28] P. Bordeenithikasem, et al., Sci. Rep. 7 (2017) 7155.
[29] Q. Zhou, et al., Acta Mater. 279 (2024) 120299.
[32] A.L. Allred, J. Inorg. Nucl. Chem. 17 (1961) 215–221.
[33] Y. Ren, et al., Sci. Bull. 69 (2024) 227–236.
[34] Y. Zhang, et al., Nat. Mater. 5 (2006) 857–860.
[35] G. Wu, et al., Nat. Commun. 15 (2024) 1223.
[36] J. Li, et al., Proc. Natl. Acad. Sci. U. S. A. 119 (2022) e2200607119.
[37] M. Ghidelli, et al., Acta Mater. 131 (2017) 246–259.
[38] A. Brognara, et al., Acta Mater. (2025) 121681.
[39] D. Hua, et al., Acta Mater. 287 (2025) 120809.
[40] M.C. Liu, et al., Acta Mater. 61 (2013) 3304–3313.
[41] N. Wang, et al., J. Alloys Compd. 973 (2024) 172874.
[42] S.F. Bojarski, et al., Scr. Mater. 279 (2026) 117278.
[43] Z. Cao, et al., J. Alloys Compd. 873 (2021) 159775.
[44] Y.F. Zhao, et al., J. Mater. Sci. Technol. 68 (2021) 16–29.
[45] G. Wu, et al., Nat. Commun. 14 (2023) 3670.
[46] M.C. Liu, et al., Scr. Mater. 61 (2009) 840–843.
[47] B.P. Sahu, et al., Phys. Rev. Mater. 6 (2022) 094002.
[48] I. Knorr, et al., Acta Mater. 61 (2013) 4984–4995.
[49] L. Huang, et al., Mater. Sci. Eng. A 831 (2022) 142277.
[50] S. Lotfian, et al., Acta Mater. 61 (2013) 4439–4451.
[51] R. Raghavan, et al., Mater. Sci. Eng. A 620 (2015) 375–382.
[52] D. Bhattacharyya, et al., Acta Mater. 59 (2011) 3804–3816.
[53] Y.F. Zhang, et al., Scr. Mater. 186 (2020) 219–224.
[54] T. Zhu, et al., MRS Bull. 34 (2011) 167–172.
[55] C. Liu, et al., Nat. Commun. 13 (2022) 1102.
[56] D. B. Williams et al., The transmission electron microscope, Springer, 1996.
[57] H. Li, et al., Nature 604 (2022) 273–279.
[58] Z. An, et al., Nature 625 (2024) 697–702.
[59] V. Sarky, et al., J. Alloys Compd. 1004 (2024) 175765.
[60] F. Khalid, et al., ChemPhysChem 25 (2024) e202400885.
[61] A.H. Cottrell, B.A. Bilby, Proc. Phys. Soc. A 62 (1949) 49–62.
[62] Q. Yu, et al., Science 347 (2015) 635–639.
[63] R.L. Fleischer, Acta Metall. 11 (1963) 203–209.
[64] Y. Ren, et al., Compos. B 263 (2023) 110833.
[65] Q. Zhou, et al., Tribol. Int. 198 (2024) 109888.
[66] X.L. Bian, et al., Acta Mater. 106 (2016) 66–77.
[67] D. Kiener, et al., Mater. Sci. Eng. A 505 (2009) 79–87.

Further reading

[30] L. Wang, et al., Phys. Rev. Lett. 105 (2010) 135501.
[31] M. Chen, et al., Science 300 (2003) 1275–1277.